Heliyon 11 (2025) e41429

Contents lists available at ScienceDirect

Heliyon

journal homepage: www.cell.com/heliyon

Research article

ANFIS-PSO analysis on axisymmetric tetra hybrid nanofluid flow of Cu-CNT-Graphene-Tio$_2$ with WEG-Blood under linear thermal radiation and inclined magnetic field: A bio-medicine application

Maddina Dinesh kumar [a,b,**], José Luis Díaz Palencia [a], G. Dharmaiah [c], A. Wakif [d], S. Noeiaghdam [e,*], U. Fernandez-Gamiz [f], S. Dinarvand [g]

[a] Department of Mathematics and Education, Universidad a Distancia de Madrid, 28400, Madrid, Spain
[b] Department of Mathematics, B V Raju Institute of Technology, Narsapur, Medak, Telangana, 502313, India
[c] Department of Mathematics, Narasaraopeta Engineering College, Narasaraopeta, India
[d] Laboratory of Mechanics, Faculty of Sciences Aïn Chock, Hassan II University, Casablanca, Morocco
[e] Institute of Mathematics, Henan Academy of Sciences, Zhengzhou, 450046, China
[f] Nuclear Engineering and Fluid Mechanics Department, University of the Basque Country UPV/EHU, Nieves Cano 12, 01006, Vitoria-Gasteiz, Spain
[g] Department of Mechanical Engineering, Central Tehran Branch, Islamic Azad University, Tehran, Iran

ARTICLE INFO

Keywords:
ANFIS-PSO
Hybrid nanofluids
MHD
Porous
Forchheimer
Linear thermal radiation

ABSTRACT

Background: The development of heat transfer devices used for heat conversion and recovery in several industrial and residential applications has long focused on improving heat transfer between two parallel plates. Numerous articles have examined the relevance of enhancing thermal performance for the system's performance and economics. Heat transport is improved by increasing the Reynolds number as the turbulent effects grow.

Applications: Regarding heat transfer, hybrid nanofluids are superior to mono nanofluids. The hybrid fluid of Cu-CNT + Graphene + TiO_2/WEG-Blood, which is subject to heat transfer in a channel between two parallel plates with an angled magnetic field and linear thermal radiation, has numerous applications in engineering, industry, and biomedical research, such as electronic cooling, drug delivery, cancer treatment, optics, missiles, satellites, transformer-electronic cooling, and military solar-equipment.

Objective: Examining the qualities of mass, flow, and heat transmission is the aim of the study of a hybrid Cu-CNT- Graphene-TiO2/WEG-Blood nanofluid as it moves via a tube of porous material that is exposed to linear thermal radiation, inclined magnetic, Forchheimer, and buoyancy influences. ANFIS-PSO model is assumed.

Method: Applying the ODE45 integration technique to the given numerical solutions yields nonlinear, non-dimensionalized, and highly partial differential equations that control the momentum, energy, and concentration. Consequently, the numerical simulation shows the concentration, velocity, and temperature profiles of the hybrid Cu-CNT- Graphene-TiO2/WEG-Blood nanofluid. A strong concordance is noted between recent and past results.

* Corresponding author.
** Corresponding author. Department of Mathematics and Education, Universidad a Distancia de Madrid, 28400 Madrid, Spain.
E-mail addresses: dineshkumar.m@bvrit.ac.in, dineshmaddina319@gmail.com (M. Dinesh kumar), joseluis.diaz.p@udima.es (J.L. Díaz Palencia), dharma.g2007@gmail.com (G. Dharmaiah), wakif.abderrahim@gmail.com (A. Wakif), snoei@hnas.ac.cn (S. Noeiaghdam), unai.fernandez@ehu.eus (U. Fernandez-Gamiz), sae.dinarvand@iauctb.ac.ir (S. Dinarvand).

https://doi.org/10.1016/j.heliyon.2024.e41429
Received 6 June 2024; Received in revised form 18 December 2024; Accepted 20 December 2024
Available online 22 December 2024

Significance and primary outcomes: Radiation regulates the microchannel temperature distribution, which significantly contributes to cooling the flow transport system, and the thermal radiation parameter shows that radiation has a retarding influence on the temperature profile.

1. Introduction

Scientists and academics are intrigued by nanofluids because of their potential advantages over conventional fluids. These fluids are more practical due to their remarkable heating and cooling characteristics. So far, efforts have focused on creating nanofluids and synthesizing nanoparticles with various factors. He et al. [1] studied ZnO−Ag saturated heat conductivity in a mixture with a 50−50 base hybrid solvent. They estimated heat conductivity using artificial neural networks. Toghraie [2] experimentally studied ternary nanofluids, a relatively novel family of materials. A variety of nanofluids, including mono, biohybrid, and ternary varieties, were used in the experiment. Water and EG are often mixed in an 80:20 ratio to form the primary fluid. Kristiawan et al. [3] used TiO2/w, to enhance helical microfin tube functionality. Scientists studied the effects of reinforcing Re on pressure drop and published their findings to improve the functionality for helical microfine using nanofluids. Kurnia et al. [4] developed and tested nanofluids in two heat exchangers, straight and helical, to transfer heat. Many studies have examined the fascinating thermal behaviour [5,6]. Researchers [7,8] reported radiation and Lorentz forces on fluid flow and the impact of hybrid nanofluids in solar energy plants. They had a lengthy discussion of the findings and agreed that the spectrum method was best for mathematically treating the models. Hybrid nanofluids are more complex forms of the more common mono-nano liquids. They incorporate evenly distributed nanoparticles traversed as host fluid, improving the resulting fluid heat conductivity. Hence, hybrid nanofluids are superior to nano liquids in terms of practicality. Multiple scholars from all around the world have recently published their findings on distinct nanofluids. Researchers have been exploring how hybrid nanofluids function in physically defined surroundings. Suction and injection were used to study a nanohybrid fluid with a permeable surface by Indumathi et al. [9]. Mburu et al. [10] examined nanofluid through boundary porous planes in a two-dimensional, incompressible, and stochastically turbulent environment. This model research made use of quasilinearisation with spectral bivariate. Shaheen et al. [11] investigated the movement of hybrid and nanofluid fluids between two parallel plates in the presence of a magnetic field and heat radiation. The numerical investigation of 3-D rotating hybrid-nanofluid has been studied by Ramana et al. in Ref. [12]. Dinarvand et al. [13] discussed an application of the mass-based hybrid nanofluid model. The study of the Bayesian regularization networks for micropolar ternary hybrid nanofluid flow [14] and the hybrid nanofluid over a nonlinear stretching surface [15], with Darcy-Forchheimer effect [16] and for comprising CNTs-Ferrousoxide/water with variable magnetic field [17] are only some limited applications of the hybrid nanofluid.

When modelling and analysing fluid flows in porous media, the laws of Darcy are often used. Forchheimer included a nonlinearized factor to permeability lowered apparent by Ref. [18]. It is called the Darcy-Forchheimer model and summarises the impacts of inertia. Muskat and Wyckoff [19] demonstrated a uniform fluid flow via a Darcy medium. Seddeek [20] investigated how thermophoresis and viscosity dissipation affect Darcy-type fluid flow, including mixed convection. In this case, the scientists found that more thermophoretic parameters cause the boundary layer to grow and the velocity to decrease. Sadiq and Hayat [21] executed magneto 2D flows over linearly expandable surface velocity with Maxwell liquid. The results show that the Prandtl number and thermal relaxation parameter have an inverse relationship with the temperature profile. Nano-Darcy fluid flow, including chemical reactions, was investigated by Hayat et al. [22]. Two horizontal plates flow a nanofluid in a Darcy-Forchheimer medium caused by a consistent magnetic field, which was studied by Rasool et al. [23]. In this article, we learn that when viscosity parameters rise, the thermal profile drops and thermophoresis and Brownian diffusion increase. Increases in surface drag force are observed at greater porosity parameter values. Various enzymes mediate the biochemical events in living systems and are of great interest to the medical sciences. Blood flow research relies heavily on in-vivo and in-vitro examinations of chemical response effects. Pulsatile blood flow via a stenosed artery was investigated by Tripathi and Sharma [24]. Many approaches have recently been used to simulate complicated aquatic resources and processing challenges, for example, the response surface approach, least squares support vectors (SVM), artificial neural networks (ANN), and artificial neural field information systems (ANFIS) by Ref. [25]. Long et al. [26] optimised artificial neural network models to forecast Al_2O_3-ethylene glycol (EG) nanofluid stability. According to prior research, when few data points are available for modelling experimental parameters, ANFIS outperforms RSM [27–29]. Li, Z.X [30] ANFIS, NN modelling, regression analysis, and experimental data on nanofluids as a secondary fluid in the refrigeration system; Selimefendigil et al. [31] for mixed convection of CNT-water nanofluid filled branching channel with an annulus and a spinning inner surface at the intersection, numerical analysis and ANFIS modelling are used, Xianqin Li et al. [32], Using a hybrid nanofluid model, the thermal improvement in heat transfer inquiry is examined. Titanium oxide and aluminium oxide nanoparticles are employed as a hybrid nanofluid. Hybrid nanoparticles are created by combining kerosene oil and water breakdown. Shuhe Sun et al. [33], by Mahantesh et al. [34] Importance of viscous and Joule heating on MoS2-Ag hybrid nanofluid heat transfer via an isothermal wedge.

1.1. Novelty of the current study

In biomedical engineering, no one has yet reported the crucial interaction between Cu-CNT-Graphene-TiO2/WEG-Blood nanoparticles. Hybrid nanofluid models using bicomponent nanoparticles in a permeable channel have yet to be explored. Authors are encouraged to examine this prospective study opportunity because of this significant research deficit/gap. The work was made more innovative using ANFIS-PSO, Inclined Magnetic, Permeable Reynolds, Porous, Forchheimer, and Linear Thermal Radiation and

Buoyancy effects to analyse the bio nanofluid's behaviour. The nano-liquid's characteristics were improved using similarity transformation principles to create a hybrid nanofluid model. A numerical approach called ODE45 was used to resolve the model. Finally, a thorough examination and discussion were conducted about the effects of the inherent physical limitations on the dynamics of the model. The ANFIS capabilities of the model were enhanced in this work by coupling it with PSO.

2. Mathematical formulation

The following governing equations are framed by using the study of Vijayalakshmi and Srinivas [35] and Hamidreza Shojaie et al. [36].

$$\frac{\partial \overline{v}}{\partial y}+\frac{\partial \overline{u}}{\partial x}=0 \tag{1}$$

$$\overline{u}\frac{\partial \overline{u}}{\partial x}+\overline{v}\frac{\partial \overline{u}}{\partial y}+\frac{\partial \overline{u}}{\partial t}=-\frac{1}{\rho_{Thnf}}\frac{\partial p}{\partial x}-\frac{\mu_{Thnf}\Phi}{\rho_{Thnf}k}\overline{u}-\frac{\sigma {B_0}^2\overline{u}}{\rho_{Thnf}}\mathrm{Cos}^2\,\Omega+\frac{\mu_{Thnf}}{\rho_{Thnf}}\left(\frac{\partial^2\overline{u}}{\partial x^2}+\frac{\partial^2\overline{u}}{\partial y^2}\right)-\frac{Cb}{x\sqrt{k}}\overline{u}^2+g(\rho\beta)_{Thnf}(T-T_u)\overline{u} \tag{2}$$

$$\overline{u}\frac{\partial \overline{v}}{\partial x}+v\frac{\partial \overline{v}}{\partial y}+\frac{\partial \overline{v}}{\partial t}=-\frac{1}{\rho_{Thnf}}\left(\frac{\partial p}{\partial y}\right)-\left(\frac{\mu_{Thnf}}{\rho_{Thnf}}\right)\left(\frac{\Phi}{k}\right)\overline{v}-\frac{\sigma {B_0}^2\overline{v}}{\rho_{Thnf}}\mathrm{Cos}^2\,\Omega+\left(\frac{\partial^2\overline{v}}{\partial x^2}+\frac{\partial^2\overline{v}}{\partial y^2}\right)\left(\frac{\mu_{Thnf}}{\rho_{Thnf}}\right)-\frac{Cb}{x\sqrt{k}}\overline{v}^2 \tag{3}$$

$$\overline{u}\frac{\partial T}{\partial x}+\overline{v}\frac{\partial T}{\partial y}+\frac{\partial T}{\partial t}=\frac{k_{Thnf}}{(\rho C_p)_{Thnf}}\left(\frac{\partial^2 T}{\partial y^2}\right)+\frac{Q_0(T-T_u)}{(\rho C_p)_{Thnf}}-\left[\frac{1}{(\rho C_p)_{Thnf}}\frac{\partial q_r}{\partial y}\right] \tag{4}$$

These are the boundary conditions involved (Kumar et al. [37])

$$at\ \overline{v}=-\overline{v}_l=-A_0\dot{h}, y=-h(t), T=T_u\ and\ \overline{u}=0, \tag{5}$$

$$at\ \overline{v}=-\overline{v}_u=-A_1\dot{h}, y=h(t), T=T_l\ and\ \overline{u}=0, \tag{6}$$

Where $A_1=\frac{\overline{v}_u}{h}$ the permeability of the wall.

Where,

$$D_2=\frac{\rho_{Thnf}}{\rho_f}, D_1=\frac{\mu_{Thnf}}{\mu_f}, D_3=\frac{k_{Thnf}}{k_f}, D_4=\frac{(\rho C_p)_{Thnf}}{(\rho C_p)_f}, D_5=\frac{(\rho\beta)_{Thnf}}{(\rho\beta_p)_f}$$

Mean flow rate functions and stream functions.

$$\overline{v}=-\psi_x, \overline{u}=\psi_y \tag{7}$$

$$\psi=\frac{\nu x f(\xi,t)}{h}, \overline{u}=\frac{\nu x}{h^2}f_\xi(\xi,t), \overline{v}=\frac{-\nu}{h}f(\xi,t). \tag{8}$$

Where $f_\xi=\left(\frac{\partial f}{\partial \xi}\right), \xi=\left(\frac{y}{h}\right)$,

The Roselands approximation for radiation can be used to simplify radiative heat transfer.

$$q_r=-\left(\frac{4\sigma}{3k}\right)\left(\frac{\partial T^4}{\partial y}\right) \tag{9}$$

Here σ is Stefan-constant. Boltzmann's k the typical absorption rate, B is the constant of the fluid and m_1 is the power law index of the temperature.

$$T^4\cong -3T_l^4+4TT_l^3, T=T_l+B\left(\frac{x}{h}\right)^{m_1}\theta(\xi) \tag{10}$$

The following is the temperature that has no dimensions.

$$\frac{T-T_l}{T_u-T_l}=\theta \tag{11}$$

The set of dimensionless governing equations has the following structure:

$$\frac{d^4f}{d\xi^4}+\alpha\left(\frac{D_1}{D_2}\right)\left[\xi\frac{d^3f}{d\xi^3}+3\frac{d^2f}{d\xi^2}\right]-M^2f'(\xi)\mathrm{Cos}^2\,\Omega+\left(\frac{D_1}{D_2}\right)\mathrm{Ref}(\xi)\frac{d^3f}{d\xi^3}-\left(\frac{D_1}{D_2}\right)\mathrm{Re}\frac{df}{d\xi}\frac{d^2f}{d\xi^2}-\frac{1}{\varepsilon}\frac{d^2f}{d\xi^2}-\mathrm{Fr}\frac{d^2f}{d\xi^2}+D_5\beta f\theta=0 \tag{12}$$

Table 1
Properties of thermophysical hybrid nanofluids.

	Standards for naming base fluids and nanoparticles	P (kg/m^3)	Cp (J/kgK)	K (W/mK)
Base fluid	WEG (Water Ethylene Glycol)	1041.89	3421.54	0.18166
	Blood	1064	3594	0.492
Tetra Hybrid Nanoparticles	TiO2	4250	690	8.953
	Graphene	2200	790	5000
	Carbon nanotubes	5100	410	3007.4
	Cu (Copper)	8933	385	400

Case-1: Nanoparticles CNT + Graphene + Cu + TiO_2 with base fluid as WEG.
Case-2: Nanoparticles CNT + Graphene + Cu + TiO_2 with base fluid as Blood.

Table 2
Dynamic viscosity, density, heat capacity, and Thermal expansion relations.

S.No	Model name	Relations
1	Dynamic viscosity	$\mu_{Thnf} = \mu_f\left\{(1-\varphi_1)^{2.5}(1-\varphi_2)^{2.5}(1-\varphi_3)^{2.5}(1-\varphi_4)^{2.5}\right\}^{-1}$
2	Density	$\rho_{Thnf} = \left\{(1-\varphi_4)\left((1-\varphi_3)\left((1-\varphi_2)\left((1-\varphi_1)+\frac{\varphi_1\rho_{s1}}{\rho_f}\right)+\frac{\varphi_2\rho_{s2}}{\rho_f}\right)+\frac{\varphi_3\rho_{s3}}{\rho_f}\right)+\frac{\varphi_4\rho_{s4}}{\rho_f}\right\}$
3	Heat Capacity	$(\rho C_p)_{Thnf} = \left\{(1-\varphi_4)\left((1-\varphi_3)\left((1-\varphi_2)\left((1-\varphi_1)+\frac{\varphi_1(\rho C_p)_{s1}}{(\rho C_p)_f}\right)+\ldots\right)+\frac{\varphi_2(\rho C_p)_{s2}}{(\rho C_p)_f}\right)+\ldots\right)+\frac{\varphi_3(\rho C_p)_{s3}}{(\rho C_p)_f}\right)+\ldots\right\}\frac{\varphi_4(\rho C_p)_{s4}}{(\rho C_p)_f}$
4	Thermal expansion	$(\rho\beta)_{Thnf} = \left\{(1-\varphi_4)\left((1-\varphi_3)\left((1-\varphi_2)\left((1-\varphi_1)+\frac{\varphi_1(\rho\beta)_{s1}}{(\rho C_p)_f}\right)+\ldots\right)+\frac{\varphi_2(\rho\beta)_{s2}}{(\rho C_p)_f}\right)+\ldots\right)+\frac{\varphi_3(\rho\beta)_{s3}}{(\rho C_p)_f}\right)+\ldots\right\}\frac{\varphi_4(\rho\beta)_{s4}}{(\rho C_p)_f}$
5	Thermal Conductivity	$\frac{k_{Thnf}}{k_f} = \frac{(k_{s4}+2k_{ternary}-2\varphi_4(k_{ternary}-k_{s4}))}{(k_{s4}+2k_{ternary}+\varphi_4(k_{ternary}-k_{s4}))}$; $\frac{k_{ternary}}{k_f} = \frac{(k_{s3}+2k_{hybrid}-2\varphi_3(k_{hybrid}-k_{s3}))}{(k_{s3}+2k_{hybrid}+\varphi_3(k_{hybrid}-k_{s3}))}$; $\frac{k_{hybrid}}{k_f} = \frac{(k_{s2}+2k_{nano}-2\varphi_2(k_{nano}-k_{s2}))}{(k_{s2}+2k_{nano}+\varphi_2(k_{nano}-k_{s2}))}$; $\frac{k_{nano}}{k_f} = \frac{(k_{s1}+2k_f-2\varphi_1(k_f-k_{s1}))}{(k_{s1}+2k_f+\varphi_1(k_f-k_{s1}))}$.

Table:3
Essential component characteristics with varying threshold values.

Key factors	Symbols	Levels		
		Low	Medium	High
Rd	Z_1	0.6	1.2	1.8
Q	Z_2	0.1	0.3	0.5
Re	Z_3	1	2	3

Table:4
Heat transfer rate experiment design and outcomes (Nusselt number).

Runs	Coded Values			Real Values			Response (Truth values)		Response (Predicted values)	
	Z_1	Z_2	Z_3	Rd	Q	Re	Nusselt number (Case-1)	Nusselt number (Case-2)	Nusselt number (Case-1)	Nusselt number (Case-2)
1	−1	−1	−1	0.6	1	0.1	1.507112	1.628931	1.414356	1.440721
2	1	−1	−1	1.8	1	0.1	1.139477	1.189272	1.111729	1. 227229
3	−1	1	−1	0.6	3	0.1	1.031011	1.046022	1.092592	1.021446
4	1	1	−1	1.8	3	0.1	1.006253	1.010052	1.089349	1.006061
5	−1	−1	1	0.6	1	0.3	1.954011	1.133793	1.712397	1. 164946
6	1	−1	1	1.8	1	0.3	1.123993	1.327019	1. 139737	1. 158393
7	−1	1	1	0.6	3	0.3	1.312926	1.541221	1.332809	1.405041
8	1	1	1	1.8	3	0.3	1.520426	1.776125	1. 483185	1. 701583
9	−1	0	0	0.6	2	0.2	1.40857	1.570875	1. 712543	1.479101
10	1	0	0	1.8	2	0.2	1.411787	1.574549	1. 666667	1. 592591
11	0	−1	0	1.2	1	0.2	1.414894	1.578106	1. 600462	1. 451282
12	0	1	0	1.2	3	0.2	1.217962	1.551612	1. 299213	1. 208289
13	0	0	−1	1.2	2	0.1	1.610561	1.287613	1. 434831	1. 522082
14	0	0	1	1.2	2	0.3	1.436942	1.581612	1.416666	1. 521221
15	0	0	0	1.2	2	0.2	1.417962	1.917343	1.330245	1.925925
16	0	0	0	1.2	2	0.2	1.417962	1.917343	1.330245	1.925925
17	0	0	0	1.2	2	0.2	1.417962	1.917343	1.330245	1.925925
18	0	0	0	1.2	2	0.2	1.417962	1.917343	1.330245	1.925925
19	0	0	0	1.2	2	0.2	1.417962	1.917343	1.330245	1.925925
20	0	0	0	1.2	2	0.2	1.417962	1.917343	1.330245	1.925925

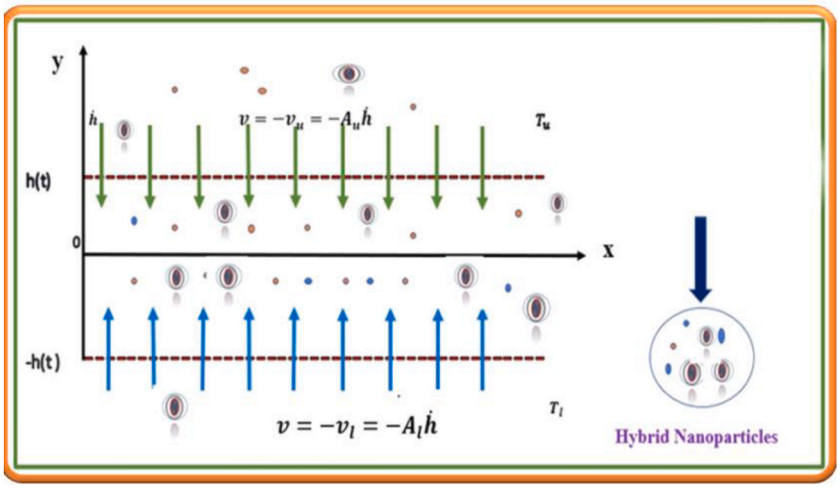

Fig:1. Physical abstract.

$$\left[\frac{D_3}{D_4}+\frac{4}{3}\frac{Rd}{D_4}\right]\frac{1}{\Pr}\frac{d^2\theta}{d\xi^2}+\alpha\left(\xi\frac{d\theta}{d\xi}+m_1\theta\right)-m_1\mathrm{Re}\frac{df}{d\xi}\theta(\xi)+\mathrm{Re}f(\xi)\frac{d\theta}{d\xi}=0 \tag{13}$$

The following are the relevant boundary conditions (Raju et al. [37]):

$$\theta(-1)=1, f(-1)=A, f'(-1)=0 \quad and\ \theta(1)=0, f'(1)=0. \tag{14}$$

The study's dimensionless parameters are

$\Pr=\frac{\mu_f(Cp)_f}{k_f}$ Prandtl number, $M=\frac{\sigma{B_0}^2}{\rho_f h}$ Magnetic parameter, $Rd=\frac{4\sigma T_0^3}{kk_f}$ Thermal Radiation

, $\varepsilon=\frac{k}{\Phi h^2}$ Darcian paraneter, $\alpha=\frac{h\dot{h}}{\nu_f}$ Wall eaxpansion ratio, $\mathrm{Re}=\frac{A\dot{h}\dot{h}}{\nu_f}$ Permeable Reynolds number,

$Q=\frac{Q_0}{(\rho cp)_f h}$ Heat source/sink, $Fr=\frac{Cb}{\sqrt{k}}$ Forchheimer number, $\beta=\frac{g\beta(T_l-T_u)}{h\overline{u}}$ Grashof number.

The following are the definitions of Nusselt number and dimensionless Skin friction (Raju et al. [37]).

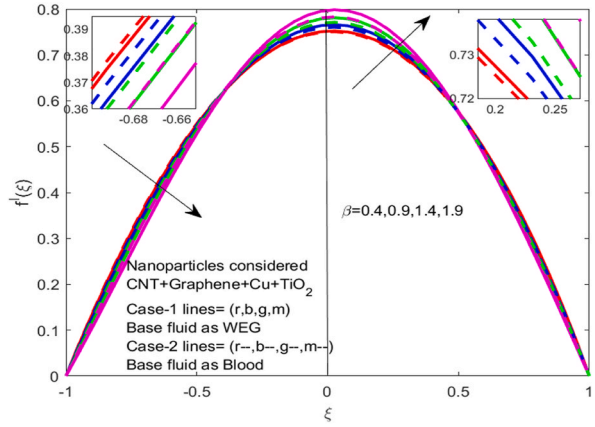

Fig:2. $f'(\xi)$ with the impact of β

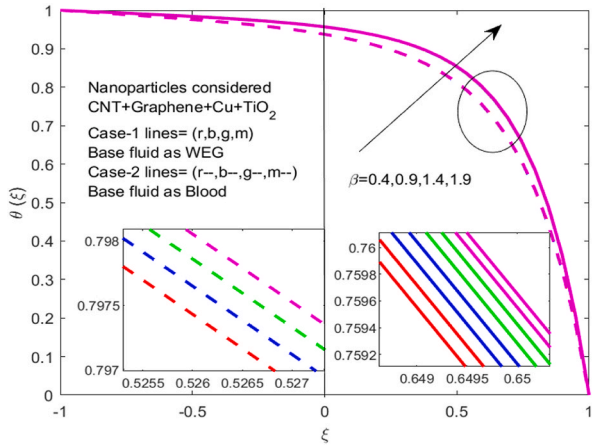

Fig:3. $\theta(\xi)$ with the impact of β

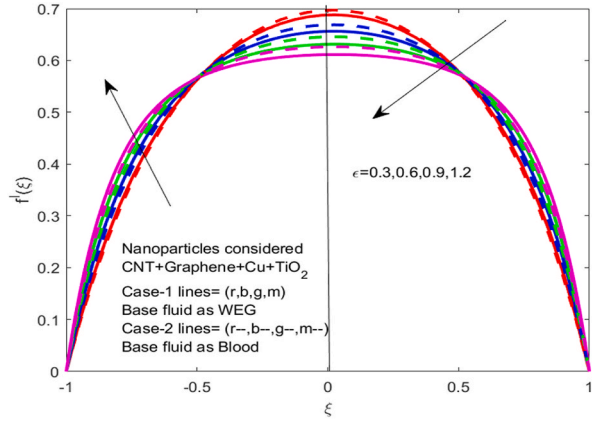

Fig:4. $f'(\xi)$ with the impact of ε

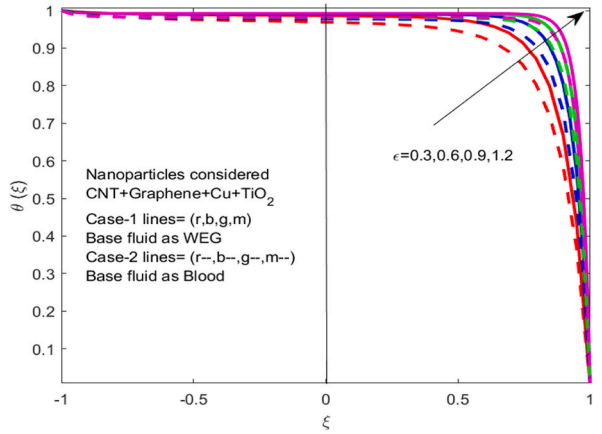

Fig:5. $\theta(\xi)$ with the impact of ε

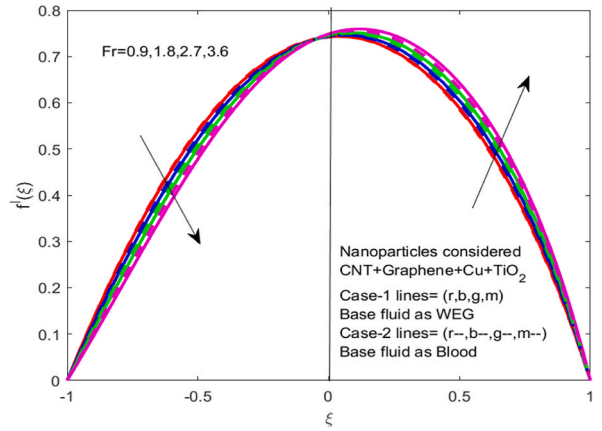

Fig:6. $f'(\xi)$ with the impact of Fr

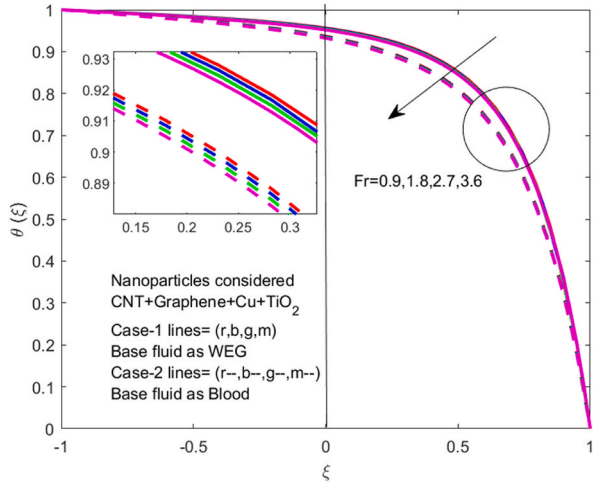

Fig:7. $\theta(\xi)$ with the impact of Fr

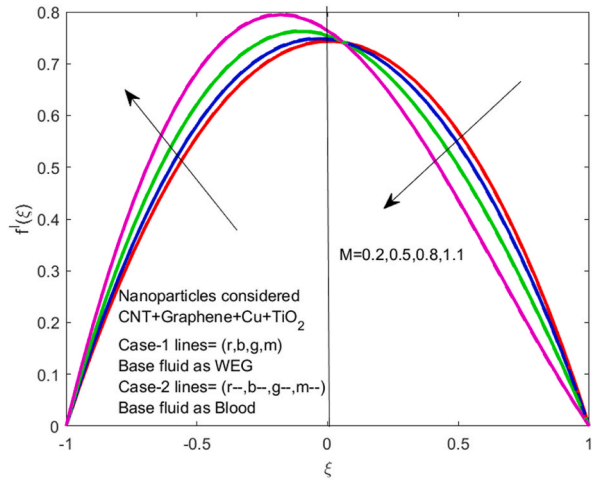

Fig:8. $f'(\xi)$ with the impact of M

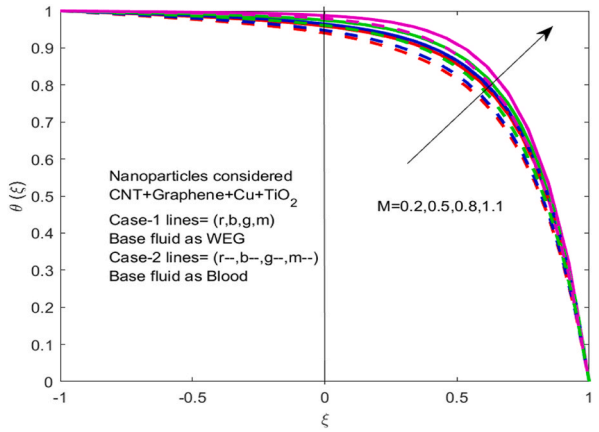

Fig:9. $\theta(\xi)$ with the impact of M

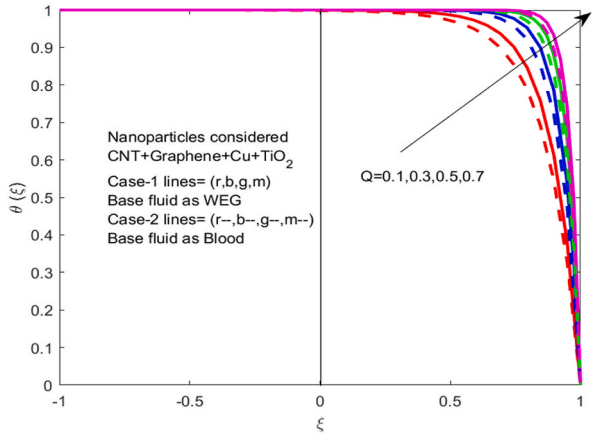

Fig:10. $\theta(\xi)$ with the impact of Q

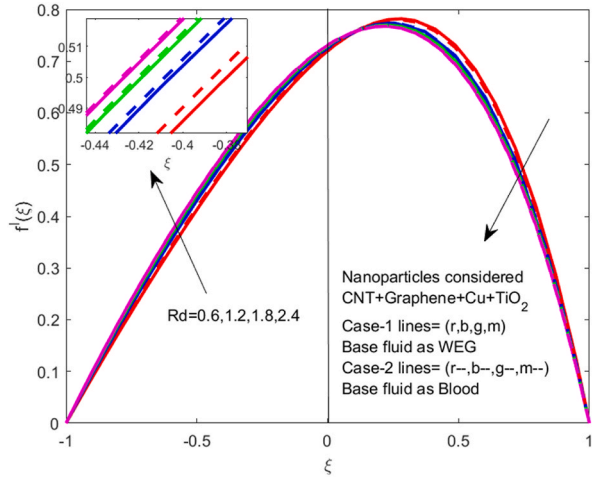

Fig:11. $f'(\xi)$ with the impact of *Rd*

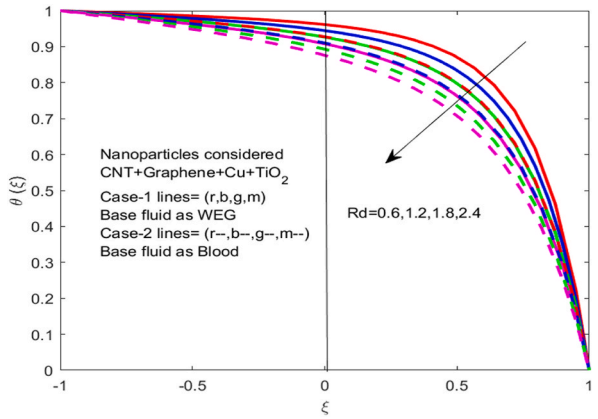

Fig:12. $\theta(\xi)$ with the impact of *Rd*

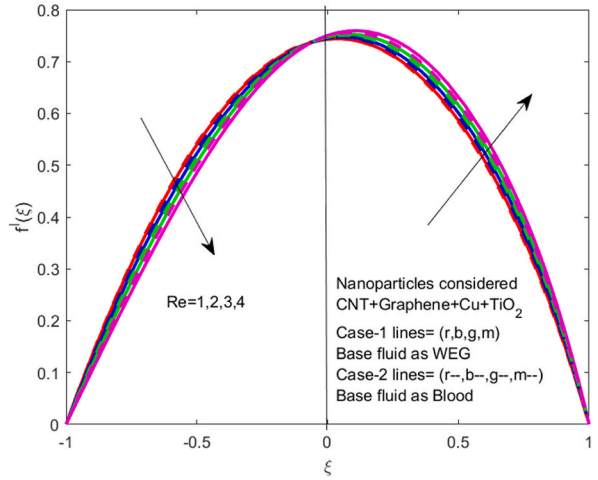

Fig:13. $f'(\xi)$ with the impact of Re

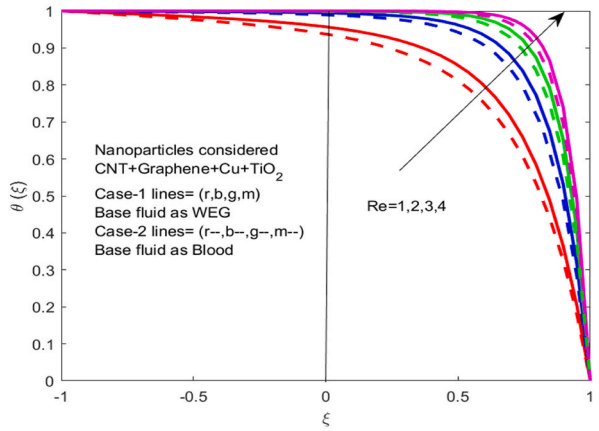

Fig:14. $\theta(\xi)$ with the impact of Re

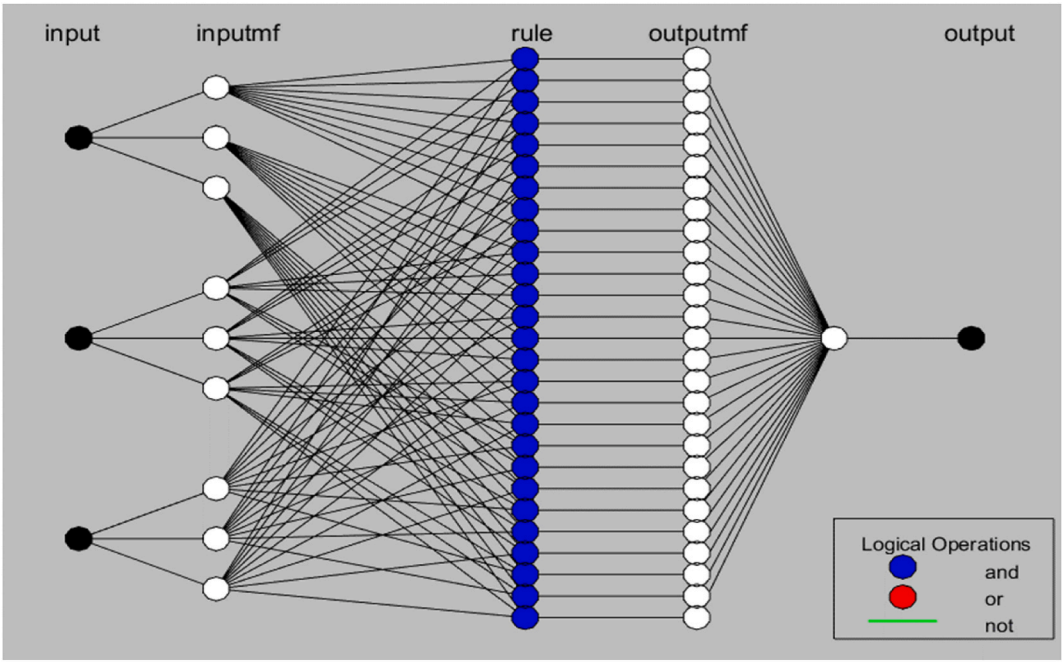

Fig:15. Neural network of ANFIS PSO-case-1, RMSE = 0.0188632.

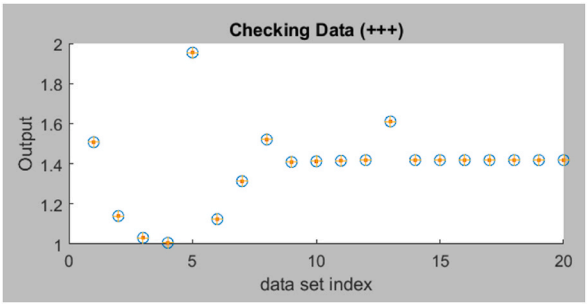

Fig:16. Training state of ANFIS PSO-Case-1.

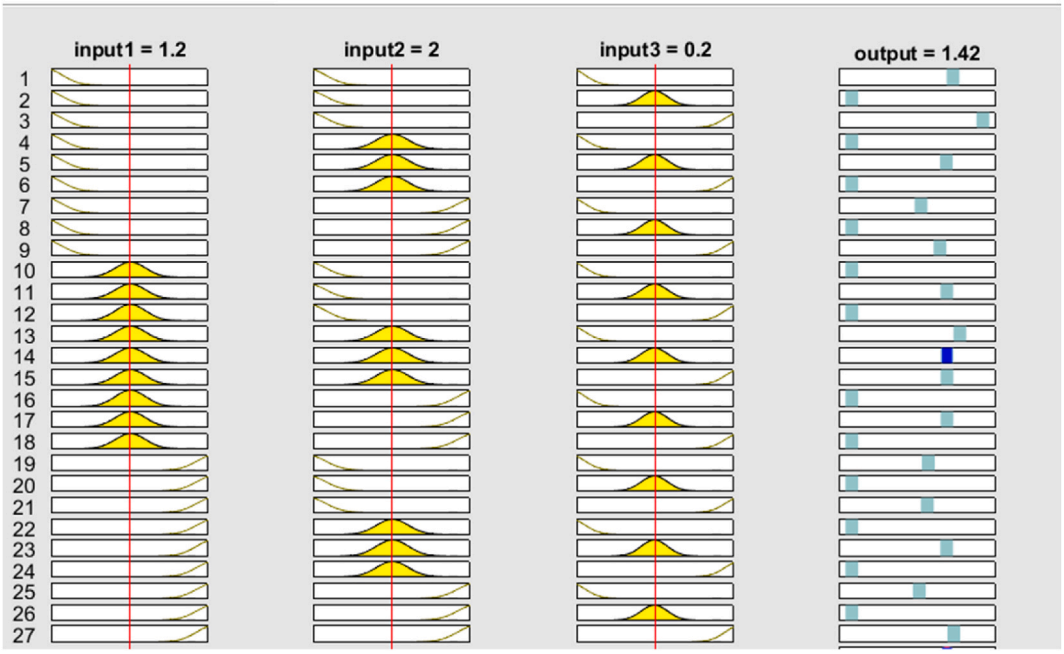

Fig:17. Rule of ANFIS-PSO Case-1.

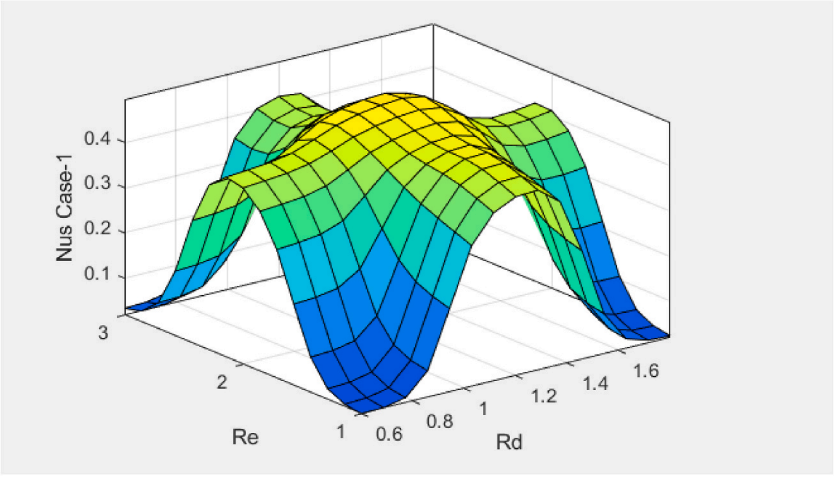

Fig: 18. Surface plot of $Nus-1$ with the impact of Re and Rd

$$Nu=-\left[D_3+\frac{4}{3}Rd\right]\theta'(\xi)_{\xi=-1,1},\ Cf_x=\frac{D_1}{D_2}f''(\xi)_{\xi=-1,1} \tag{15}$$

Once the flow field has been identified, the momentum equation (3) can be modified to get the normal pressure gradient by adding the velocity component.

$$\begin{aligned}&\frac{\partial p}{\partial y}=-\frac{\rho_{Thnf}}{\rho_f}\left[\alpha\left(f+yf_y\right)Re^{-1}+ff_y+\frac{\mu_{Thnf}}{\rho_{Thnf}}\frac{1}{\nu_f}Re^{-1}f_{yy}-\frac{\sigma{B_0}^2\overline{v}}{\rho_{Thnf}}-\frac{Cb}{x\sqrt{k}}\overline{v}^2\right],\\&p=\frac{\overline{p}}{\rho_f\nu_w^2}.\end{aligned} \tag{16}$$

It is now possible to find the normal pressure distribution by integrating equation (16), letting p_c be the centre line pressure. Acknowledging that $ff_y=\frac{1}{2}(f^2)'$ and $\left(f+yf_y\right)=(yf)'$, hence (Hamidreza Shojaie et al. [36]):

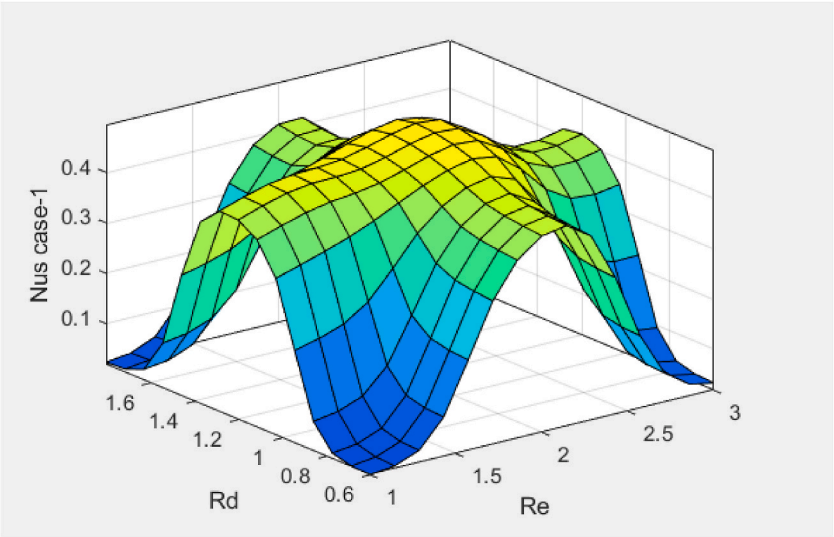

Fig: 19. Surface plot of *Nus* − 1 with the impact of *Rd* and Re

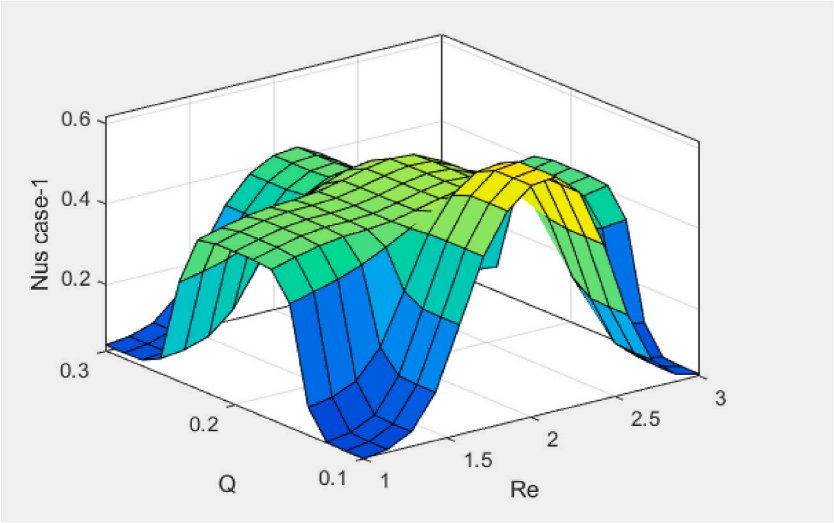

Fig: 20. Surface plot of *Nus* − 1 with the impact of *Q* and Re

$$\int_{p_c}^{p(y)} dp = \int_0^y -\frac{\rho_{Thnf}}{\rho_f}\left[\frac{\alpha}{\mathrm{Re}}(yf)' + \left(\frac{f^2}{2}\right)' + \frac{\mu_{Thnf}}{\rho_{Thnf}}\frac{1}{\nu_f}\mathrm{Re}^{-1}f'' - \frac{\sigma {B_0}^2 \bar{v}}{\rho_{Thnf}} - \frac{Cb}{x\sqrt{k}}\bar{v}^2\right]dy \tag{17}$$

Normal pressure will be as follows (Hamidreza Shojaie et al. [36]):

$$\Delta p_n = -\frac{\rho_{Thnf}}{\rho_f}\left[\frac{\alpha}{\mathrm{Re}}(yf) + \left(\frac{f^2}{2} - \frac{f^2(0)}{2}\right)\right] - \frac{\mu_{Thnf}}{\mu_f}\left(\frac{1}{\mathrm{Re}}(f' - f'(0))\right) - \frac{1}{\rho_f}M^2[f - f(0)]\mathrm{Cos}^2\,\Omega - D_2 Fr[f'' - f''(0)]. \tag{18}$$

3. The numerical solution and dimensionless equations' dependability

Using MATLAB built-in function ODE45. The modified equations 12 and 13 are solved for conditions (14) using ODE45. In order to accomplish this, we need to assume the following:

$$f = h_1, \theta = h_5, \chi = h_6, \chi' = h_7, f' = h_2, \theta' = h_6, f'' = h_3, f''' = h_4.$$

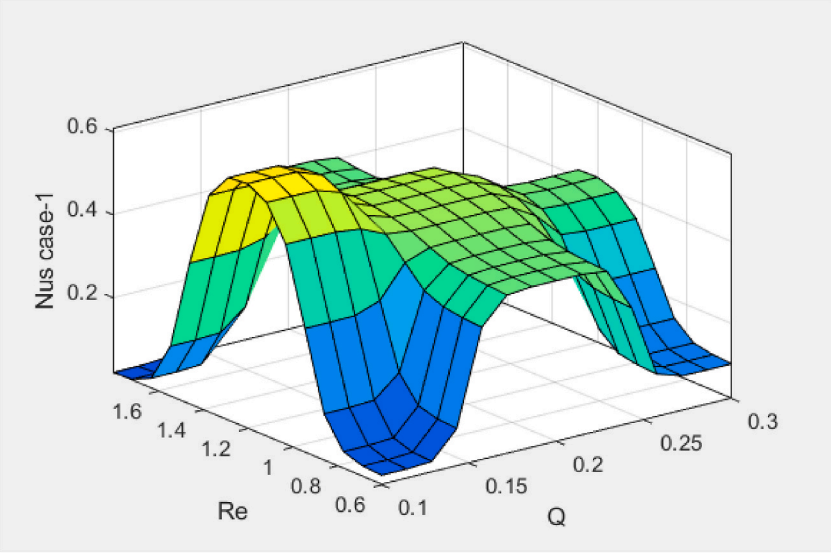

Fig: 21. Surface plot of *Nus* – 1 with the impact of Re and *Q*

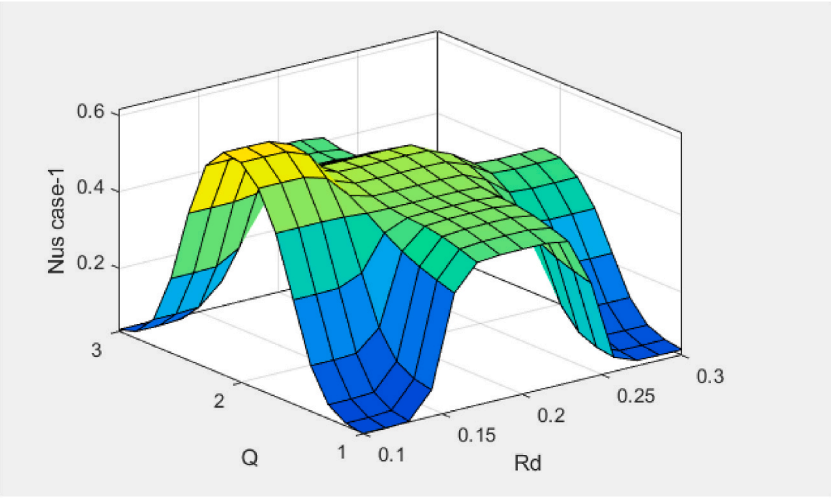

Fig: 22. Surface plot of *Nus* – 1 with the impact of *Q* and *Rd*

3.1. Making use of boundary conditions

$$f_a(1) = A, f_a(6), f_a(2) = 0, f_a(5) = 1$$
$$f_b(1) = 1, f_b(6), f_b(2) = 0, f_b(5) = 0.$$

4. Results and discussion section

4.1. Various dimensionless parameters impact on the velocity, Temperature and Concentration profile

This section discusses various dimensionless parameters' impact on the Velocity, Temperature and Concentration profiles in cases. **First Case**: Nanoparticles CNT + Graphene + Cu + TiO_2 with base fluid as WEG. **Second Case**: Nanoparticles CNT + Graphene + Cu + TiO_2 with base fluid as Blood. Evaluation of the properties is done using the bvp4c method. The range of parameters are: $0.4 \leq \beta \leq 1.9$; $0.3 \leq \varepsilon \leq 1.2$; $0.9 \leq Fr \leq 3.6$; $0.2 \leq M \leq 1.1$; $0.1 \leq Q \leq 0.7$; $0.6 \leq Rd \leq 2.4$; $1.0 \leq Re \leq 4.0$.Table:1illustrates the Thermophysical properties of the Nanoparticles and base fluid, and Table:2 depicts the physical properties relations of Dynamic viscosity, density, heat capacity, and Thermal expansion relations; Table:3 shows Important component attributes with different threshold values; Table:4

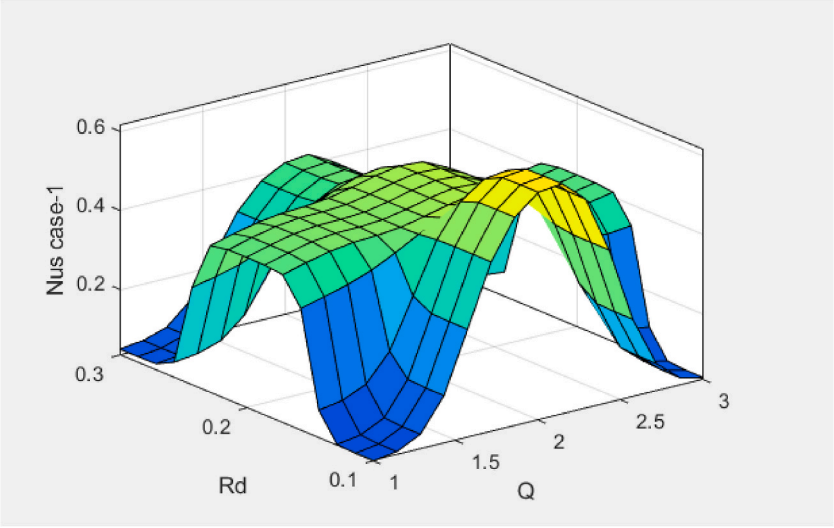

Fig:23. Surface plot of *Nus* − 1 with the impact of *Rd* and *Q*

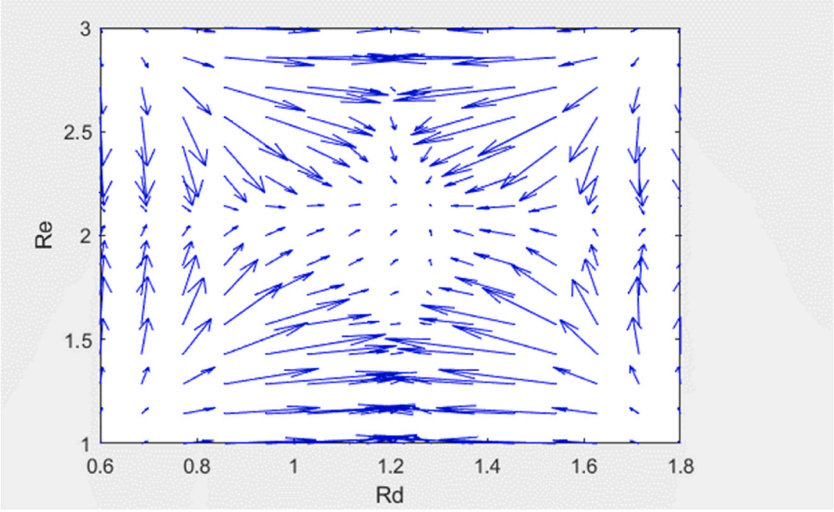

Fig:24. Quiver plot of *Nus* − 1 with the impact of Re and *Rd*

illustrates the design and results of a heat transfer rate experiment (Nusselt number). Fig:1 represents the physical model of the current study. Figs. 2 and 3 show the f ’(ξ) and θ(ξ) profiles for various values of β for both group-I (CNT + Graphene + Cu + TiO_2 with base fluid as WEG) and group-II (CNT + Graphene + Cu + TiO_2 with base fluid as Blood). From Fig. 2, when the value of β enhances, f ’(ξ) is high at the middle of the momentum wall, and fluid flow behaviour is graphically symmetrical. From figure-3, when the value of β enhances, θ(ξ) significantly increases for both group-I (CNT + Graphene + Cu + TiO_2 with base fluid as WEG) and group-II (CNT + Graphene + Cu + TiO_2 with base fluid as Blood), due to high enhancement in the thickness of the permeable boundary layers for group-II (CNT + Graphene + Cu + TiO_2 with base fluid as Blood). In axisymmetric flow, buoyancy forces become more prominent as the Grashof number rises, producing a mixed velocity profile with forced and natural convection effects. Stronger convective heat transfer is responsible for the enhanced thermal boundary layer development, as the rising temperature indicates (see Table 2).

Figs. 4–5 reflect the f ’(ξ), θ(ξ) distributions for varying values of ‘ε’ for both group-I (CNT + Graphene + Cu + TiO_2 with base fluid as WEG) and group-II (CNT + Graphene + Cu + TiO_2 with base fluid as BLOOD). From fig-4, when the value of ‘ε’ enhances, f ’(ξ) is high at the middle of the momentum wall, and fluid flow behaviour is graphically symmetrical. From fig-5, when the value of ‘ε’ enhances, θ(ξ) significantly increases for both group-I (CNT + Graphene + Cu + TiO_2 with base fluid as WEG) and group-II (CNT + Graphene + Cu + TiO_2 with base fluid as Blood), due to high enhancement in the thickness of the permeable boundary layers for group-II (CNT + Graphene + Cu + TiO_2 with base fluid as Blood) from lower plate to upper plate. The temperature profile rises due to enhanced heat retention as the Darcy parameter increases in an axisymmetric flow, the concentration profile falls as increased fluid flow lowers the reactant concentration, and the velocity profile displays mixed behaviour due to varying resistance in the porous

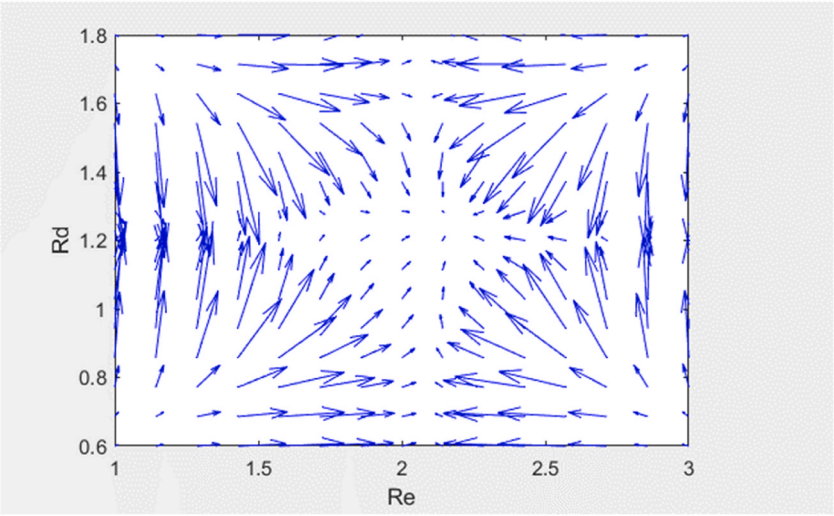

Fig:25. Quiver plot of *Nus* − 1 with the impact of *Rd* and Re

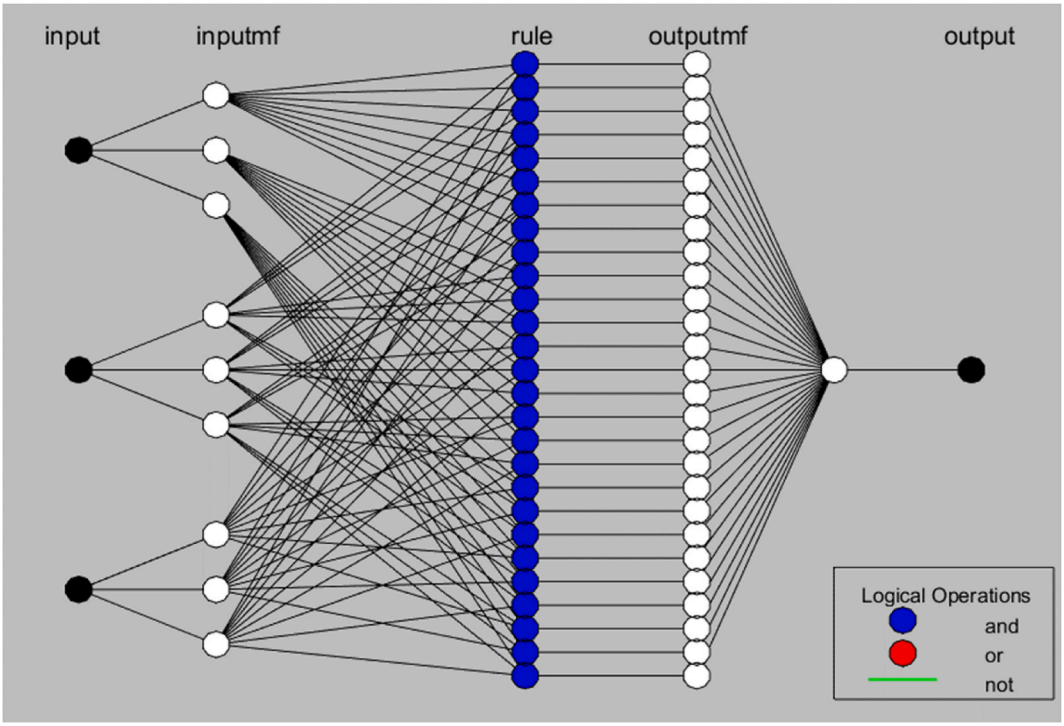

Fig: 26. Neural network of ANFIS PSO-case-2, RMSE = 0.0180985.

medium. Figs. 6–7 related to 'Fr' on f '(ξ), θ(ξ) distributions, with $0.9 \leq Fr \leq 3.6$. Fig-6 demonstrated the 'Fr' parameter impact on f '(ξ). It is noted that the 'Fr' value raises f '(ξ) decreased at the regime's lower surface and increased at its upper surface. From θ(ξ) distributions (7), lower and upper boundaries fall. The temperature profile drop as the Forchheimer parameter grows in an axisymmetric flow because the increased resistance to flow decreases heat transfer and reactant distribution in the medium.

In contrast, the velocity profile shows mixed behaviour because of nonlinear drag effects. Figs. 8–9 related to 'M' on f '(ξ)and θ(ξ) distributions, with $0.2 \leq M \leq 1.1$. Fig-8 demonstrated the 'M' parameter impact on f '(ξ). It is noted that the 'M' value raises f '(ξ), declines at the upper regime surface and falls at the lower regime surface. Physically, by increasing the magnetic parameter, Lorentz forces are produced, decreasing the fluid momentum. From θ(ξ) distribution (9 fig), both lower and upper boundaries significantly improved. The temperature rises as the magnetic field increases, resulting in higher temperatures. In contrast, the velocity profile in an

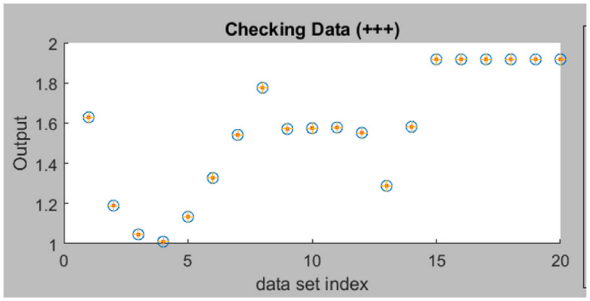

Fig:27. Training state of ANFIS PSO-Case-2.

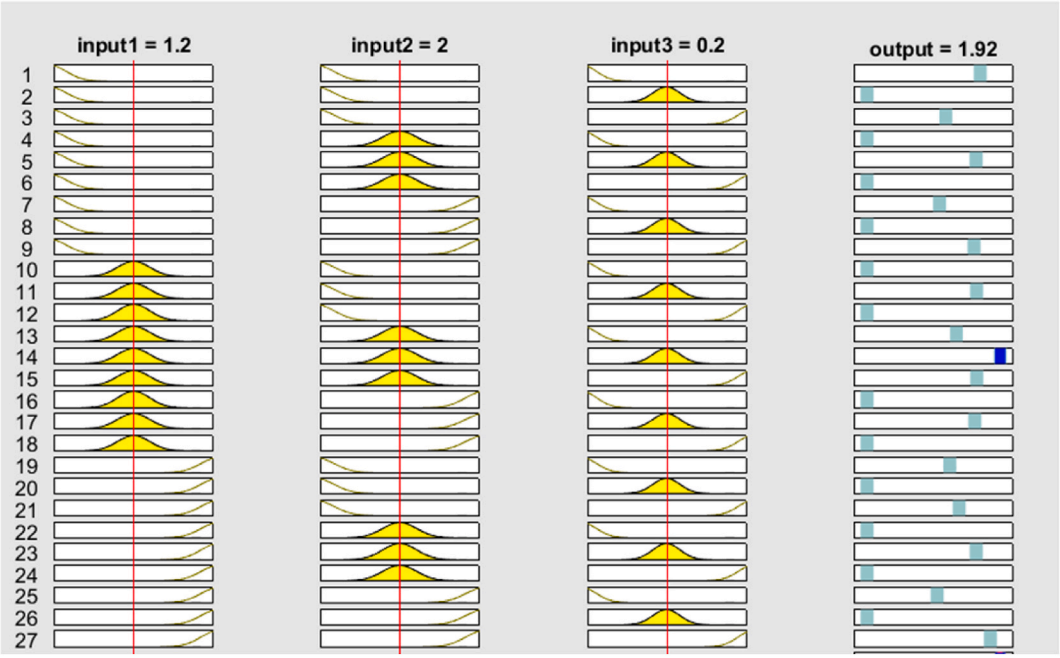

Fig:28. Rule of ANFIS-PSO Case-2.

axisymmetric flow exhibits mixed behaviour as the magnetic parameter increases because the Lorentz force modifies fluid motion. Fig. 10 illustrates $\theta(\xi)$ profile with the impact of Q, It is noted, that the $\theta(\xi)$ profile is increasing as Q raises, and the combined nanofluids pose dominant behaviour in CNT + Graphene + Cu + TiO2 with base fluid as WEG temperature relative to CNT + Graphene + Cu + TiO_2 with base fluid as Blood. The temperature profile rises when the heat source/sink parameter increases in an axisymmetric flow because either the lower heat sink slows down cooling, which raises temperatures, or the extra heat source increases energy inside the system, raising temperatures overall. Figs. 11–12 related to 'Rd' impact on f '(ξ), θ(ξ) distributions. Fig. 11 depicts the velocity profile Firmly; the fluid velocity increases at the lower surface and decreases at the upper regime as Rd increases. Moreover, in the f '(ξ) of CNT + Graphene + Cu + TiO_2 with base fluid as Blood, the channel's upper section is more prominent than its lower section. CNT + Graphene + Cu + TiO_2 with base fluid as WEG.Fig:12 shows the impact of *Rd* on θ(ξ), it is noticed that θ(ξ) profile is decreasing if the *Rd* parameter values raise means. The complex interaction between radiative heat loss and fluid motion causes the velocity profile in an axisymmetric flow to exhibit mixed behaviour as the radiation parameter increases. Meanwhile, the temperature profile decreases as increased radiation intensifies energy loss from the system, resulting in lower temperatures. Figs. 13 and 14 related to 'Re' impact on f '(ξ), θ(ξ)distributions of both group-I (CNT + Graphene + Cu + TiO_2 with base fluid as WEG) and group-II (CNT + Graphene + Cu + TiO_2 with base fluid as Blood). By raising 'Re', both θ(ξ) distributions are enhanced in the channel and CNT + Graphene + Cu + TiO_2 with base fluid, as WEG dominates both profiles, f '(ξ) profile has mixed nature. The temperature profile rises in an axisymmetric flow as the permeable Reynolds number increases because improved flow facilitates better heat and mass transfer, which raises temperatures. The velocity profile exhibits mixed behaviour because of the porous medium's interaction between inertial and viscous forces (see Fig. 17).

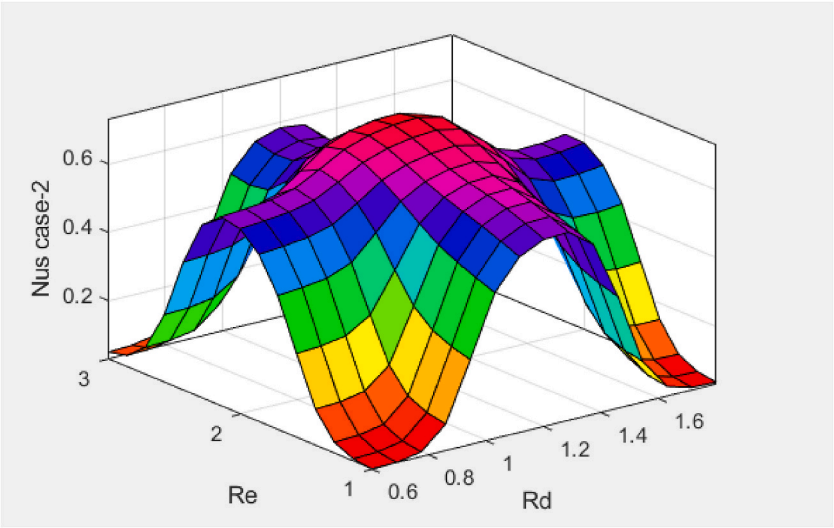

Fig:29. Surface plot of *Nus* – 2 with the impact of Re and *Rd*

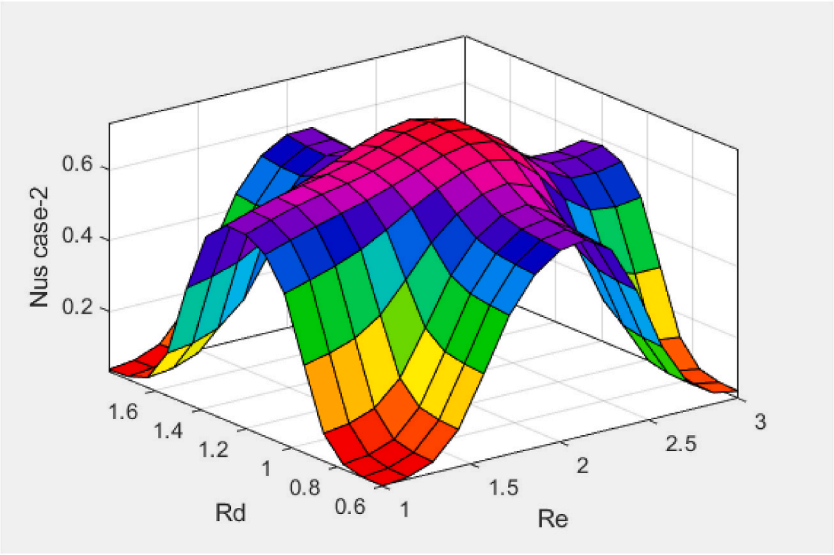

Fig:30. Surface plot of *Nus* – 2 with the impact of *Rd* and Re

4.2. Adaptive neuro-fuzzy inference system approach and particle swarm optimization algorithm (ANFIS-PSO)

Adaptive Neuro-Fuzzy Inference System (ANFIS) and Particle Swarm Optimization (PSO) are combined in ANFIS-PSO to improve the ANFIS model's parameters, improving the model's efficiency and accuracy of predictions. It uses PSO's ability to identify the best answers in challenging search environments. Fig. 15 represents RMSE of Neural Network is 0.0188632 for Nanoparticles CNT + Graphene + Cu + TiO_2 with base fluid as WEG case, respectively. Fig:16 Training state of ANFIS PSO-Case-1, Fig:17 Rule of ANFIS-PSO Case-1 Figs. 18 and 19 depict response surface 3-D plots for Nusselt number with Re (1–3) and Rd (0.6–1.6) parameter impacts for Nanoparticles CNT + Graphene + Cu + TiO_2 with base fluid as WEG case. From this figure, we have noticed the maximum output of Nu_x is coming when Re = 2.0 and Rd = 1.2 for Nanoparticles CNT + Graphene + Cu + TiO_2 with base fluid as WEG case and vice-versa. Figs. 20 and 21 depict response surface 3-D plots for Nusselt number with Re (0.6–1.6) and Q (0.1–0.3) parameter impacts for Nanoparticles CNT + Graphene + Cu + TiO_2 with base fluid as WEG case. From this figure, we have noticed the maximum output of Nux is coming when Re = 1.4 and Q = 0.2 for Nanoparticles CNT + Graphene + Cu + TiO_2 with base fluid as WEG case and vice-versa. Figs. 22 and 23 depict response surface 3-D plots for Nusselt number with Q (1–3) and Rd (0.1–0.3) parameter impacts for Nanoparticles CNT + Graphene + Cu + TiO_2 with base fluid as WEG case. From this figure, we have noticed the maximum output of Nux is coming when Q = 2.0 and Rd = 0.2 for Nanoparticles CNT + Graphene + Cu + TiO_2 with base fluid as WEG case and vice-versa.

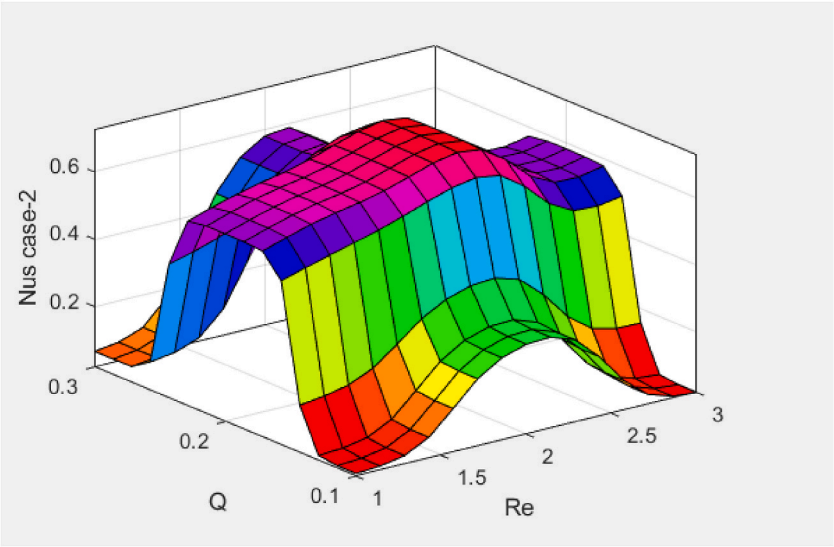

Fig:31. Surface plot of *Nus* – 2 with the impact of *Q* and Re

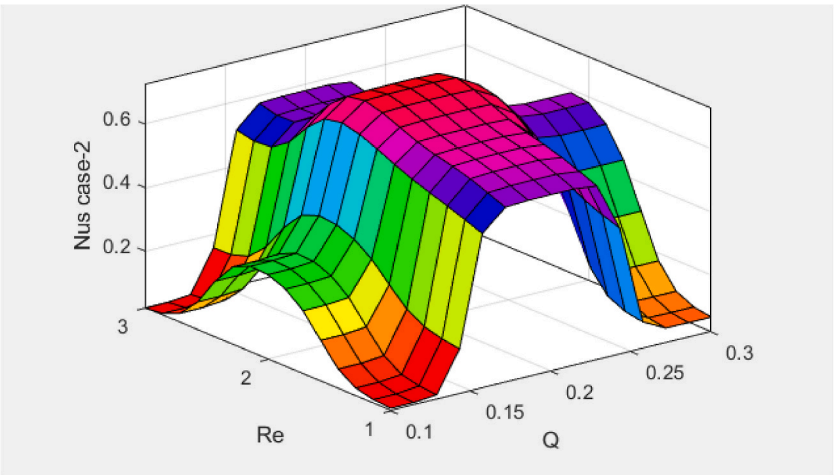

Fig:32. Surface plot of *Nus* – 2 with the impact of Re and *Q*

Figs. 24 and 25 depicted Quiver plot for Nusselt number with (Re, Rd), (Rd, Re) parameter impacts for Nanoparticles CNT + Graphene + Cu + TiO_2 with base fluid as WEG case and vice-versa, These Quiver plots are useful to predict the flow pattern of the fluid.

Fig. 26 represents RMSE of Neural Network is 0.0180985 for Nanoparticles CNT + Graphene + Cu + TiO_2 with base fluid as Blood case, Fig:27 Training state of ANFIS PSO-Case-2, Fig:28 Ruleof ANFIS-PSO Case-2, Figs. 29 and 30 depict response surface 3-D plots for Nusselt number with Re (1–3) and Rd (0.6–1.6) parameter impacts for Nanoparticles CNT + Graphene + Cu + TiO_2 with base fluid as Blood case. From this figure, we have noticed the maximum output of Nux comes when Re = 2.0 and Rd = 1.2 for nanoparticles CNT + Graphene + Cu + TiO2 with base fluid as a blood case and vice versa. Figs. 31 and 32 depict response surface 3-D plots for Nusselt number with Re (0.6–1.6) and Q (0.1–0.3) parameter impacts for Nanoparticles CNT + Graphene + Cu + TiO_2 with base fluid as Blood case. From this figure, we have noticed the maximum output of Nux comes when Re = 1.4 and Q = 0.2 for nanoparticles CNT + Graphene + Cu + TiO2 with base fluid as a blood case and vice versa. Figs. 33 and 34 depict response surface 3-D plots for Nusselt number with Q (1–3) and Rd (0.1–0.3) parameter impacts for Nanoparticles CNT + Graphene + Cu + TiO_2 with base fluid as Blood case. From this figure, we have noticed the maximum output of Nux comes when Q = 2.0 and Rd = 0.2 for nanoparticles CNT + Graphene + Cu + TiO2 with base fluid as a blood case and vice versa. Vector fields are represented graphically in quiver plots, where arrows, or quivers, show the direction and magnitude of vectors at specific grid locations. They frequently display electromagnetic fields, fluid flow, and other vector fields in physics and engineering. Figs. 35 and 36 depict Quiver plot for Nusselt number with (Re, Rd), (Rd, Re) parameter impacts for Nanoparticles CNT + Graphene + Cu + TiO2 with base fluid as Blood case and vice-versa; these plots are useful to predict the flow pattern of the fluid (see Fig. 27).

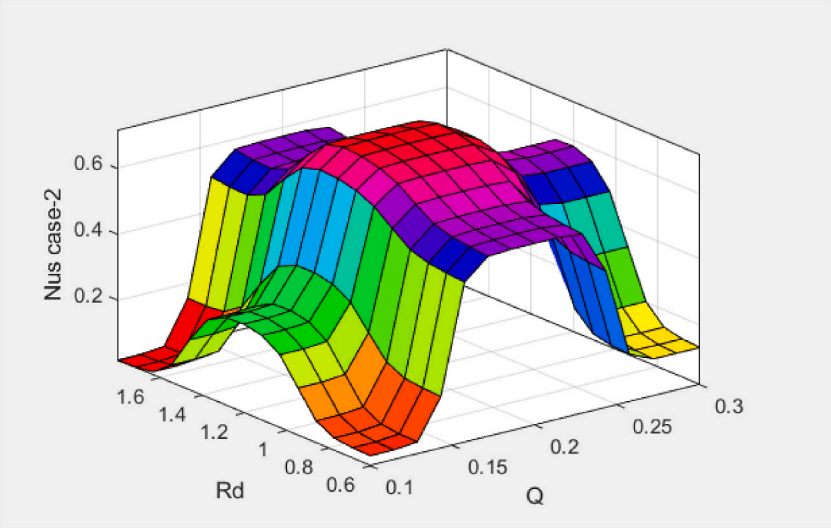

Fig:33. Surface plot of *Nus* − 2 with the impact of *Rd* and *Q*

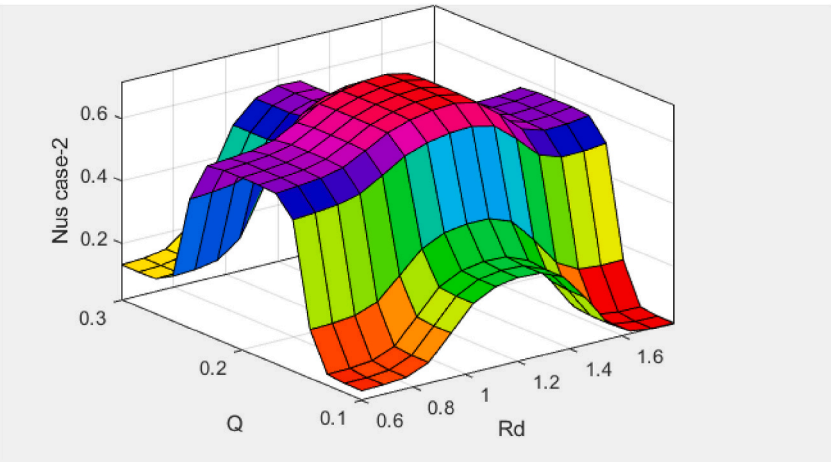

Fig:34. Surface plot of *Nus* − 2 with the impact of *Q* and *Rd*

5. Conclusion

The crucial connection between Cu-CNT- Graphene-TiO_2/WEG-BLOOD nanoparticles in biomedical engineering was established in the current work. Unexplored are hybrid nanofluid models that employ bicomponent nanoparticles in a permeable channel. Because of this substantial research gap or deficit, authors are encouraged to investigate this potential research opportunity. Utilising ANFIS-PSO, Inclined Magnetic, Permeable Reynolds, Porous, Forchheimer, Linear Thermal Radiation, and Buoyancy effects to analyse the behaviour of the bio nanofluid made the task more inventive. The model was solved using the ODE45 numerical method. Finally, a detailed analysis and discussion of how the inherent physical restrictions affect the dynamics of the model were conducted. The model's ANFIS capabilities were improved by coupling with PSO in this work.

5.1. Significant outcomes of the present study

- $\theta(\xi)$ Profile grows when the values of the Q, M parameters are raised.
- $\theta(\xi)$ Profile declines during the moment when the Fr, Rd values rise.
- $\chi(\xi)$ profile increases when the parameter M, Re values rise.
- $\chi(\xi)$ Profile decreases when the parameter Fr values are raised.
- $f'(\xi)$ The profile's nature is mixed when the parameter values increase ε, Fr, M, Rd, Re.

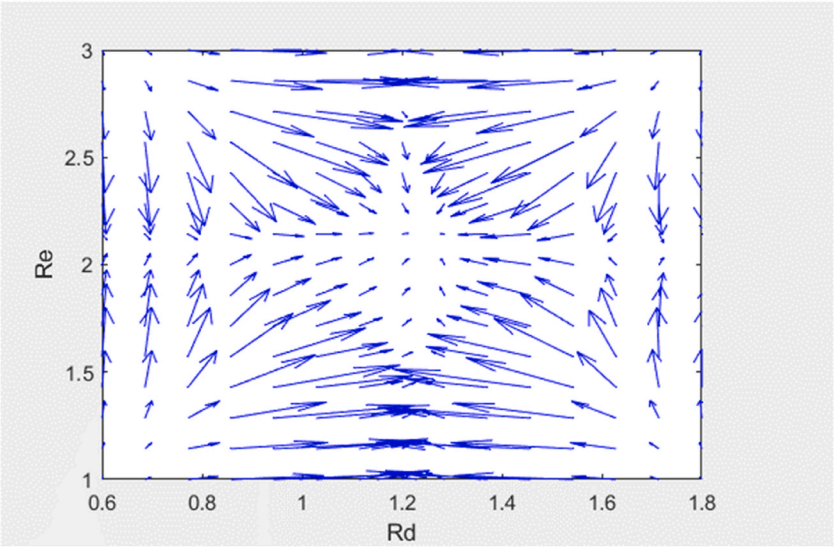

Fig:35. Quiver plot of *Nus* – 2 with the impact of Re and *Rd*

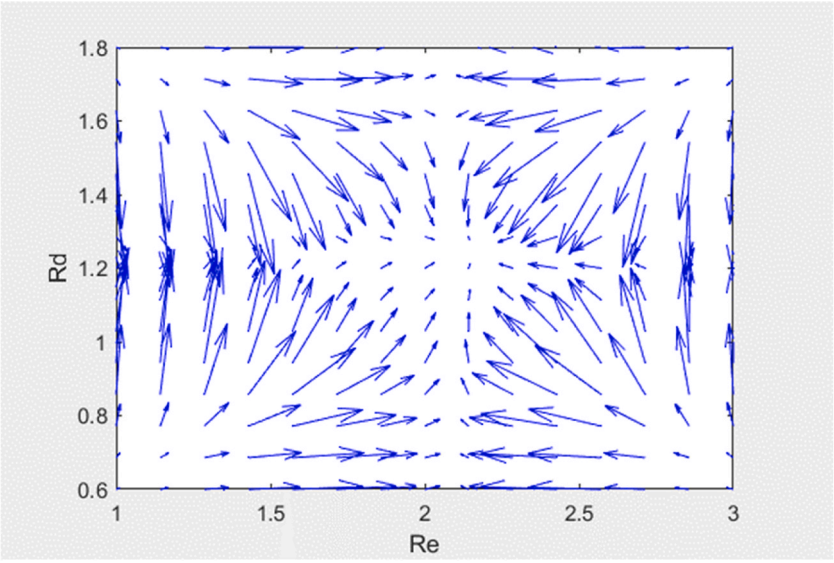

Fig:36. Quiver plot of *Nus* – 2 with the impact of *Rd* and Re

- The obtained RMSE values for the ANFIS-PSO, which are 0.01888632 in case-1 and 0.0180985 in case-2, show the accuracy and fit of the current model.

5.2. Applications of the current study

- **Bio-Medical Imaging Enhancement:**

The optimised model improves MRI clarity by examining the interaction between hybrid nanofluids and blood under thermal and magnetic circumstances. Better treatment results and more precise diagnosis are the results of this.

- **Targeted Drug Delivery Systems**

This research contributes to regulating the circulatory behaviour of nanoparticles, improving the accuracy of targeted medication administration. This can significantly increase therapeutic efficacy, especially in cancer therapy.

- **Thermal Therapy Techniques**

By forecasting heat transport in blood arteries under linear thermal radiation, the analysis can maximize the benefits of thermal treatment. This improves the effectiveness and safety of therapies such as cryotherapy and heat.

- **Blood Flow Management in Medical Devices**

Understanding blood flow under thermal and magnetic forces is one way the model helps design medical equipment. In controlling blood clots and vascular disorders, in particular, this enhances device performance.

CRediT authorship contribution statement

Maddina Dinesh kumar: Writing – review & editing, Writing – original draft, Validation, Software, Investigation. **José Luis Díaz Palencia:** Writing – review & editing, Validation, Software, Methodology, Formal analysis. **G. Dharmaiah:** Writing – review & editing, Software, Methodology, Formal analysis. **A. Wakif:** Writing – review & editing, Validation, Methodology. **S. Noeiaghdam:** Writing – review & editing, Methodology, Investigation, Formal analysis. **U. Fernandez-Gamiz:** Writing – review & editing, Validation, Resources, Investigation. **S. Dinarvand:** Writing – review & editing, Methodology, Investigation.

Data availability statement

Data will be made available on reasonable request.

Funding

Funding U.F.-G. was supported by the Mobility Lab Foundation, a governmental organization of the Provincial Council of Araba and the local council of Vitoria-Gasteiz. S. Noeiaghdam was supported by the Henan Academy of Sciences (Project No. 241819246).

Declaration of competing interest

The authors declare that they have no known competing financial interests or personal relationships that could have appeared to influence the work reported in this paper.

References

[1] W. He, B. Ruhani, N. Izadpanahi, N.N. Esfahani, A. Karimipour, M. Afrand, Using of artificial neural networks (ANNs) to predict the thermal conductivity of zinc Oxide−Silver (50%−50%)/water hybrid Newtonian nanofluid, Int. Commun. Heat Mass Transfer 116 (No) (2020) 104645.
[2] D. Toghraie, A comprehensive experimental investigation of thermal conductivity of a ternary hybrid nanofluid containing MWCNTs- titania-zinc oxide/water ethylene glycol (80:20) as well as binary and mono nanofluids, Synth. Met. 268 (2020) 116501.
[3] B. Kristiawan, A.I. Rifa'i, K. Enoki, A.T. Wijayanta, T. Miyazaki, Enhancing the thermal performance of TiO2/water nanofluids flowing in a helical microfin tube, Powder Technol. 376 (2020) 254–262.
[4] J.C. Kurnia, B. Chaedir, A.T. Wijayanta, A.P. Sasmito, Convective heat transfer enhancement of laminar Herschel−Bulkley non-Newtonian fluid in straight and helical heat exchangers with twisted tape inserts, Ind. Eng. Chem. Res. 61 (2022) 814–844.
[5] M.M. Bhatti, O.A. Bég, R. Ellahi, M.H. Doranehgard, F. Rabiei, Electro-magnetohydrodynamics hybrid nanofluid flow with gold and magnesium oxide nanoparticles through vertical parallel plates, J. Magn. Magn Mater. 564 (2022) 170136.
[6] S.M. Sait, M.A. Sheremet, H. Oztop, Thermal analysis and entropy generation of magnetic Eyring-Powell nanofluid with viscous dissipation in a wavy asymmetric channel, Int. J. Numer. Methods Heat Fluid Flow (2022) 1609–1636.
[7] M.B. Muhammad, F.O. Hakan, E. Rahmat, Study of the magnetized hybrid nanofluid flow through a flat elastic surface with applications in solar energy, Materials 15 (7507) (2022).
[8] L. Zhang, N. Tariq, M.B. Mubashir, Study of nonlinear quadratic convection on magnetised viscous fluid flow over a non-Darcian circular elastic surface via spectral approach, J. Taibah Univ. Sci. 17 (2023) 2183702.
[9] N. Indumathi, B. Ganga, R. Jayaprakash, A.K.A. Hakeem, Heat transfer of hybrid-nanofluids flow past a permeable flat surface with different volume fractions. J, Appl. Comput. Mech. (2022) 21–35.
[10] Z.M. Mburu, S. Mondal, P. Sibanda, An unsteady nanofluid flow past parallel porous plates: a numerical study, Nanosci. Nanotechnology. 12 (2022) 41–55.
[11] A. Shaheen, M. Imran, H. Waqas, M. Raza, S. Rashid, Thermal transport analysis of squeezing hybrid nanofluid flow between two parallel plates, Adv. Mech. Eng. 15 (2023) 1–15.
[12] R. Mohana Ramana, C. Maheswari, S. Mohiddin Shaw, G. Dharmaiah, U. Fernandez-Gamiz, S. Noeiaghdam, Numerical investigation of 3-D rotating hybrid nanofluid Forchheimer flow with radiation absorption over a stretching sheet, Results in Engineering 22 (2024) 102019, https://doi.org/10.1016/j.rineng.2024.102019.
[13] S. Dinarvand, M. Behrouz, S. Ahmadi, P. Ghasemi, S. Noeiaghdam, U. Fernandez-Gamiz, Mixed convection of thermomicropolar AgNPs-GrNPs nanofluid: an application of mass-based hybrid nanofluid model, Case Stud. Therm. Eng. 49 (2023) 103224, https://doi.org/10.1016/j.csite.2023.103224.
[14] Bhupendra K. Sharma, P. Sharma, N.K. Mishra, S. Noeiaghdam, U. Fernandez-Gamiz, Bayesian regularization networks for micropolar ternary hybrid nanofluid flow of blood with homogeneous and heterogeneous reactions: entropy generation optimization, Alex. Eng. J. 77 (2023) 127–148, https://doi.org/10.1016/j.aej.2023.06.080.
[15] N. Hameed, S. Noeiaghdam, W. Khan, B. Pimpunchat, U. Fernandez-Gamiz, M. Sohail Khan, A. Rehman, Analytical analysis of the magnetic field, heat generation and absorption, viscous dissipation on couple stress Casson hybrid Nano fluid over a nonlinear stretching surface, Results in Engineering https://doi.org/10.1016/j.rineng.2022.100601.
[16] M.S. Khan, S. Mei, Shabnam, U. Fernandez-Gamiz, S. Noeiaghdam, A. Khan, Numerical simulation of a time-dependent electroviscous and hybrid nanofluid with Darcy-forchheimer effect between squeezing plates, Nanomaterials 12 (2022) 876, https://doi.org/10.3390/nano12050876.

[17] M.S. Khan, S. Mei, Shabnam, U. Fernandez-Gamiz, S. Noeiaghdam, S.A. Shah, A. Khan, Numerical analysis of unsteady hybrid nanofluid flow comprising CNTs-ferrousoxide/water with variable magnetic field, Nanomaterials 12 (2022) 180, https://doi.org/10.3390/nano12020180.
[18] P. Forchheimer, Wasserbewegung durch boden, Z. Ver, Deutsch Ing. 45 (1901) 1782–1788.
[19] M. Muskat, R. Wyckoff, The Flow of Homogeneous Fluids through Porous Media, JW Edwards, Michigan, Ann Arbor, 1937.
[20] M. Seddeek, Influence of viscous dissipation and thermophoresis on Darcy–Horkheimer mixed convection in a fluid saturated porous media, J. Colloid Interface Sci. 293 (1) (2006) 137–142.
[21] M.A. Sadiq, T. Hayat, Darcy–Horkheimer flow of magneto maxwell liquid bounded by convectively heated sheet, Results Phys. 6 (2016) 884–890.
[22] T. Hayat, F. Shah, M.I. Khan, A. Alsaedi, Framing the performance of heat absorption/generation and thermal radiation in chemically reactive Darcy-Horkheimer flow, Results Phys. 7 (2017) 3390–3395.
[23] G. Rasool, W.A. Khan, S.M. Bilal, I. Khan, MHD squeezed Darcy–Forchheimer nanofluid flow between two h–distance apart horizontal plates, Open Phys. 18 (1) (2020) 1100–1107.
[24] Tripathi Bhavya, Kumar Sharma Bhupendra, Two-phase analysis of blood flow through a stenosed artery with the effects of a chemical reaction and radiation, Ric, Mat 73 (2024) 151–177.
[25] H. Rajabi Kuyakhi, R.T. Boldaji, M. Azadian, Light hydrocarbons solvents solubility modelling in bitumen using learning approaches, Petrol. Sci. Technol. 39 (4) (2021) 115–131.
[26] L. Li, Y. Zhai, Y. Jin, J. Wang, H. Wang, M. Ma, Stability, thermal performance and artificial neural network modelling of viscosity and thermal conductivity of Al2O3- ethylene glycol nanofluids, Powder Technol. 363 (2020) 360–368.
[27] R. Tahmasebi Boldaji, H. Rajabi Kuyakhi, N. Tahmasebi Boldaji, M. Rajabzadeh, S. Rashidi, M. Torki, S. Ghazanfari, A comparative study of mathematical and ANFIS models to determine the effect of ultrasonic waves on the viscosity of crude oil, Petrol. Sci. Technol. 40 (2) (2022) 150–165.
[28] H. Rajabi Kuyakhi, R. Tahmasebi Boldaji, Developing an adaptive neuro-fuzzy inference system based on particle swarm optimisation model for forecasting Cr (VI) removal by NiO nanoparticles, Environ. Prog. Sustain. Energy 40 (4) (2021) e13597.
[29] R.T. Boldaji, H.R. Kuyakhi, Predicting supercritical extraction of st. John's wort by simple quadratic polynomial model and adaptive neuro-fuzzy inference system firefly algorithm, Journal of Analytical Techniques and Research 3 (2) (2021) 14–27.
[30] Z.X. Li, F.L. Renault, A.O.C. Gómez, M.M. Sarafraz, H. Khan, M.R. Safaei, E.P.B. Filho, Nanofluids as secondary fluid in the refrigeration system: experimental data, regression, ANFIS, and NN modelling, Int. J. Heat Mass Transf. 144 (2019) 118635.
[31] F. Selimefendigil, H.F. Öztop, Numerical analysis and ANFIS modelling for mixed convection of CNT-water nanofluid-filled branching channel with an annulus and a rotating inner surface at the junction, Int. J. Heat Mass Tran. 127 (2018) 583–599.
[32] X. Li, A. Abbasi, K. Al-Khaled, H.F.M. Ameen, S.U. Khan, M.I. Khan, W. Farooq, G. Rasool, K. Guedri, Thermal performance of iron oxide and copper (Fe3O4, Cu) in the hybrid nanofluid flow of Casson material with Hall current via the complex wavy channel, Mater. Sci. Eng., B 289 (2023) 116250.
[33] S. Sun, M.I. Khan, K. Al-Khaled, A. Raza, S.S. Abdullaev, S.U. Khan, N. Tamam, S.M. Eldin, Prabhakar fractional approach for enhancement of heat transfer due to hybrid nanomaterial with sinusoidal heat conditions, Case Stud. Therm. Eng. 49 (2023) 103240.
[34] B. Mahanthesh, S.A. Shehzad, T. Ambreen, S.U. Khan, Significance of Joule heating and viscous heating on heat transport of MoS 2–Ag hybrid nanofluid past an isothermal wedge, Journal of Thermal Analysis and Calorimetry 143 (2021) 1221–1229.
[35] A. Vijayalakshmi, S. Srinivas, Asymmetric nanofluid flow between expanding or contracting permeable walls with thermal radiation, Frontiers in Heat and Mass Transfer 7 (10) (2016) 1–11.
[36] H. Shojaie Chahregh, S. Dinarvand, TiO2-Ag/blood hybrid nanofluid flow through an artery with drug delivery applications and blood circulation in the respiratory system, Int. J. Numer. Methods Heat Fluid Flow 30 (11) (2020) 4775–4796.
[37] C.S.K. Raju, N.A. Ahammad, K. Sajjan, N.A. Shah, S.J. Yook, M.D. Kumar, Nonlinear movements of axisymmetric ternary hybrid nanofluids in a thermally radiated expanding or contracting permeable Darcy Walls with different shapes and densities: simple linear regression, Int. Commun. Heat Mass Tran. 135 (2022) 106110.